



MOF-derived nitrogen doped carbon modified g-C₃N₄ heterostructure composite with enhanced photocatalytic activity for bisphenol A degradation with peroxyomonosulfate under visible light irradiation



Yan Gong^{a,b,e}, Xu Zhao^{b,*}, Hui Zhang^c, Bo Yang^{a,e,***}, Ke Xiao^{a,b,e}, Tao Guo^{a,b,e}, Juanjuan Zhang^b, Huixin Shao^b, Yanbing Wang^d, Gang Yu^d

^a College of Chemistry and Environmental Engineering, Shenzhen University, Shenzhen 518060, PR China

^b Key Laboratory of Drinking Water Science and Technology, Research Center for Eco-Environmental Sciences, Chinese Academy of Sciences, Beijing 100085, PR China

^c State Key Laboratory of Environmental Chemistry and Eco-toxicology, Research Centre for Eco-Environmental Sciences, Chinese Academy of Sciences, Beijing 100085, PR China

^d School of Environment, POPs Research Center, Tsinghua University, Beijing 100084, PR China

^e Shenzhen Key Laboratory of Environmental Chemistry and Ecological Remediation, Shenzhen University, Shenzhen 518060, PR China

ARTICLE INFO

Keywords:

Photocatalysis
g-C₃N₄
MOF
Peroxyomonosulfate
BPA

ABSTRACT

Designing metal-free g-C₃N₄ based photocatalytic system with efficient photocatalytic activity has received enormous attention in the field of environmental remediation because of its great potential for removing refractory contaminants. Herein, a novel metal organic framework (ZIF-8)-derived nitrogen doped carbon (ZIF-NC) modified g-C₃N₄ heterostructured composite was synthesized through a facile thermal treatment method. Benefiting from the hierarchical porosity, conductive network, and abundant exposed active sites for peroxyomonosulfate (PMS) activation of MOF-derived nitrogen doped carbon, the introduction of MOF-derived nitrogen doped carbon into g-C₃N₄ not only facilitates the charge separation of g-C₃N₄ but also greatly accelerates PMS activation to yield high active SO₄^{·-} radical. The energy band diagrams derived from Mott-Schottky, valence band X-ray photoelectron spectroscopy and ultraviolet photoelectron spectroscopy studies indicate that the formed heterojunction between g-C₃N₄ and ZIF-NC is Schottky type. The ZIF-NC with lower Fermi level energy can serve as an excellent electron acceptor to enable fast electron transfer from the conduction band of g-C₃N₄ to ZIF-NC and boost the charge separation of g-C₃N₄. Photoelectrochemical tests combined with multiple spectroscopic techniques further confirm the enhanced charge carrier separation performance of composite. As a result, the as-prepared hybrids displayed remarkably improved photocatalytic activities toward bisphenol A (BPA) degradation in the presence of PMS under visible light irradiation. The apparent rate constant, k, for BPA degradation of the ZIF-NC/g-C₃N₄ composites with PMS is approximately 8.6 times as high as that of bare g-C₃N₄. This work provides a promising approach on the rational design of high-performance, cost-effective photocatalysts for environmental remediation.

1. Introduction

Graphitic carbon nitride (g-C₃N₄) has garnered interest in environmental purification, primarily because of its peculiar inherent two-dimensional (2D) crystal structure, visible-light response ability (band gap ~2.7 eV) and excellent chemical stability [1–5]. Recent works demonstrate that g-C₃N₄ can be used as heterogeneous catalyst for activation of peroxyomonosulfate to generate strong sulfate radicals (SO₄^{·-}) (PMS) by the photoinduced electrons under visible light irradiation [6–12]. Compared with hydroxyl radicals (·OH), the sulfate

radicals has been regarded as an efficient active radical for oxidation of refractory pollutant due to the significant advantages associated with high oxidative potential (2.5–3.1 V vs SHE), wide working pH range (2–8) and long half-life (30–40 μs) [13–16]. The intrinsic metal-free nature without secondary contamination concern and robust stability make g-C₃N₄ emerged as a promising material for SO₄^{·-} production under visible light irradiation. However, the activation efficiency of PMS by the photoexcited g-C₃N₄ is far from satisfactory due to the relatively sluggish photoinduced charge separation, insufficient light absorption and limited surface active sites for PMS activation. In an

* Corresponding author.

** Corresponding author at: College of Chemistry and Environmental Engineering, Shenzhen University, Shenzhen 518060, PR China.

E-mail addresses: zhaoxu@rcees.ac.cn (X. Zhao), boyang@szu.edu.cn (B. Yang).

effort to promote the activation efficiency of PMS by $\text{g-C}_3\text{N}_4$, it is highly desirable to develop a more efficient $\text{g-C}_3\text{N}_4$ based photocatalyst system for $\text{SO}_4^{\cdot-}$ production under visible light irradiation.

Recent studies have revealed that nanocarbon materials show attractive catalytic activity in PMS activation to yield $\text{SO}_4^{\cdot-}$ [17–20]. The large surface area, unique surface chemistry property and metal-free nature of nanocarbon materials make them promising alternative to metal-based catalysts in environmental remediation. What's more, it has been reported that doping nitrogen atom into the carbon matrixes could greatly improve their catalytic performance towards PMS activation. The doped nitrogen could not only increase the surface basicity for PMS adsorption, but also facilitate electron transfer reaction with PMS by activating the neighboring sp^2 carbon atoms [21,22]. In particular, the nitrogen doped porous carbon obtained from thermal treatment of the parent MOF template has been demonstrated as efficient catalyst for triggering the active reaction of PMS to yield $\text{SO}_4^{\cdot-}$. The MOF-derived carbon materials exhibit lots of distinct merits, such as hierarchical porous structures, large surface areas and abundant active sites, which benefit the promotion of catalytic performance of PMS activation. Wang et al. [21] reported the nitrogen doped porous carbon synthesized from carbonization of a nitrogen-rich metal-organic framework (ZIF-8) exhibited excellent PMS activation to produce high active $\text{SO}_4^{\cdot-}$ for phenol degradation. In addition, the carbon matrix obtained by graphitization upon preparation at high temperature possesses outstanding electrical conductivity, which is favorable for the charge transfer.

Previous studies [23–26] has demonstrated that coupling $\text{g-C}_3\text{N}_4$ with various nanocarbon materials can facilitate the photoinduced charge separation and broaden light response range, result in enhancing the photocatalytic activity of $\text{g-C}_3\text{N}_4$. Thus, it is reasonable to assume that the integration of MOF-derived nitrogen doped carbon (MOF-NC) and $\text{g-C}_3\text{N}_4$ is an efficient way to promote the PMS activation ability and photocatalytic activity of $\text{g-C}_3\text{N}_4$. In this regard, the formed heterojunction composite would possess the following advantages: (i) enhanced light harvesting can be achieved by incorporating MOF-NC into the $\text{g-C}_3\text{N}_4$ matrix; (ii) the formed junction between $\text{g-C}_3\text{N}_4$ and MOF-NC can accelerate charge transfer across the interface and shortens the charge transport distance, which would boost the photogenerated carrier separation; (iii) the abundant active sites on the surface of MOF-NC can facilitate the PMS activation, which is beneficial to yield $\text{SO}_4^{\cdot-}$. However, to the best of our knowledge, there is no systematic study on this novel MOF-NC/ $\text{g-C}_3\text{N}_4$ composite with efficient PMS activation for organic pollutant removal.

Herein, taking the ZIF-8-derived nitrogen doped carbon (ZIF-NC) and $\text{g-C}_3\text{N}_4$ as a proof of concept, we report the fabrication of ZIF-NC/ $\text{g-C}_3\text{N}_4$ composite through a facile thermal treatment method. Such hybrid composite offered a broadening optical window for effective light harvesting, efficient interfacial charge separation, as well as abundant surface active sites for PMS activation. As a result, the composite are anticipated to exhibit extremely high photocatalytic activities toward bisphenol A (BPA) degradation with PMS under visible light irradiation.

2. Experimental

2.1. Synthesis of $\text{g-C}_3\text{N}_4$

All starting materials were reagent grade and used without further purification. For the synthesis of $\text{g-C}_3\text{N}_4$, 5 g of melamine was placed in a semi-closed porcelain crucible with a cover and heated up to 550 °C for 4 h at a rate of 5 °C/min. After reaction, the porcelain crucible was cooled down to room temperature. The collected yellow solid was grinded into powders.

2.2. Synthesis of ZIF-8

The ZIF-8 was prepared in methanol according to the documented

method [21]. In a typical procedure, 0.558 g $\text{Zn}(\text{NO}_3)_2 \cdot 6\text{H}_2\text{O}$ was dissolved in 30 ml methanol, which was subsequently added into 30 ml methanol containing 0.616 g 2-methylimidazole with vigorous stirring for 24 h at room temperature. The as-obtained precipitates were centrifuged and washed with methanol three times and dried at 60 °C for 24 h under vacuum.

2.3. Synthesis of ZIF-NC

The as-synthesized ZIF-8 powder was placed in a tube furnace under Ar gas flow and heated up to 1000 °C (5 °C/min), and maintained at 1000 °C for 5 h. The result black products were ground into powder to get the final ZIF-NC.

2.4. Synthesis of ZIF-CN/ $\text{g-C}_3\text{N}_4$ composites

An appropriate amount of ZIF-CN in a methanolic solution was firstly placed in an ultrasonic bath for 30 min to completely disperse the ZIF-NC. Then $\text{g-C}_3\text{N}_4$ powder was added into the above solution and stirred for 24 h. After volatilization of the methanol in water bath at 60 °C, the obtained powder was heated to 300 °C for 2 h under Ar atmosphere. According to this method, different mass ratios of ZIF-NC/ $\text{g-C}_3\text{N}_4$ composites at 0.01%, 0.1%, 0.5%, 0.75% and 1% were synthesized and denoted as 0.01% ZIF-NC/ $\text{g-C}_3\text{N}_4$, 0.1% ZIF-NC/ $\text{g-C}_3\text{N}_4$, 0.5% ZIF-NC/ $\text{g-C}_3\text{N}_4$, 0.75% ZIF-NC/ $\text{g-C}_3\text{N}_4$ and 1% ZIF-NC/ $\text{g-C}_3\text{N}_4$.

2.5. Characterization

The phase identification of the samples was performed by X-ray diffractometer (X'pert Pro MPD) with $\text{Cu K}\alpha$. The morphology and microstructure of the samples were observed by a field emission scanning electron microscope (FESEM, Hitachi SU-8020, Japan) and transmission electron microscopy (TEM, Hitachi H7500, Japan). The high resolution TEM (HRTEM) images were obtained on a JEOL JEM-2100F microscope at 200 kV. The element states of the samples were detected by X-ray photoelectron spectroscopy (XPS, ESCALAB 250Xi, Thermo Fisher Scientific) and the surface functional groups were detected by Fourier transform infrared spectrophotometer (FT-IR, VERTEX 70, Bruker). Raman spectra were performed with a confocal Raman microscope (LabRAM HR 800, Horiba) equipped with an Ar laser (514 nm). UV-vis absorption spectra were recorded on a Hitachi 3010 spectrophotometer. The steady-state photoluminescence (PL) spectra were measured using a Hitachi F-4500 under the excitation of 350 nm. PL decay curves of the samples were measured at room temperature on a Transient/steady State Fluorescence Spectrometer (F900, Edinburgh Instruments, UK) with an excitation wavelength of 350 nm.

The photoelectrochemical measurements were carried out in a conventional three-electrode cell by using a CHI 660 B (Shanghai, China) electrochemical workstation. Pt wire was used as a counter electrode, a saturated calomel electrode (SCE) was used as a reference electrode. The electrolyte was aqueous 0.05 M Na_2SO_4 . The working electrode was irradiated with visible light obtained from a 300 W Xe lamp (BoPhilae technology Co., LTD, Beijing) with 420 nm cutoff filter. Chopped-light amperometric I-t characterizations were evaluated under chopped light irradiation. Electrochemical impedance spectroscopy (EIS) was conducted by applying an AC voltage amplitude of 5 mV within the frequency range from 10^5 to 0.01 Hz with 50 mM Na_2SO_4 . The electron spin resonance (ESR) signals of spin-trapped oxidative radicals were obtained on a Bruker EMX A300-10/12 spectrometer with 5,5-dimethyl-1-pyrroline-*N*-oxide (DMPO) as spin-trapping agents.

2.6. Evaluation of photocatalytic activity

The photocatalytic performances of samples were evaluated by degradation of BPA with initial concentration of 20 mg/L under visible light irradiation. A 300 W Xenon lamp with an optical filter

($\lambda > 400$ nm) was employed as solar light source. Before irradiation and addition of PMS, the sample was dispersed into 50 mL of BPA aqueous solution with magnetic stirring for 1 h in the dark to reach the absorption–desorption equilibrium. After desired intervals, 0.8 mL samples were taken with adding methanol to quench the radicals and filtered with a 0.22 M organic phase filter to separate the supernatant liquid from catalysts for analysis. A HPLC (Shimadzu, DGU-20A3R(C), Japan) with column C18 and a UV detector was used to detect the concentration change of BPA during the reaction, the temperature of C18 separation column was 30 °C and the detection wavelength was set as 230 nm. The mobile phase was methanol: water (60:40), and flow rate was 1 mL/min.

The experiments of active species radical capture were carried out by employing *t*-butanol (TBA), methanol (MeOH), ethylenediamine tetraacetic acid disodium salt (EDTA-2Na) and p-benzoquinone (BQ) as the scavenger for hydroxyl radical, $\text{SO}_4^{\cdot-}$, hole and $\cdot\text{O}_2^{\cdot-}$, respectively.

3. Results and discussion

3.1. Characterizations of ZIF-NC/g-C₃N₄ composites

The fabrication of the ZIF-NC/g-C₃N₄ hybrid composite involved a two-step process, as shown in Fig. 1. Briefly, ZIF-NC was firstly obtained by carbonization of ZIF-8 at 1000 °C under Ar atmosphere. Then a predefined mass ratio of the as-prepared ZIF-NC and g-C₃N₄ were dispersed in methanol under sonication for 0.5 h, and the precipitates obtained by filtration were heated at 300 °C in Ar gas to form the final hybrid composite.

The SEM images in Fig. 2a reveal that the as-synthesized ZIF-8 nanocrystals are composed of rhombic dodecahedra structure with uniform size in 350 nm scale. After carbonization of the host ZIF-8 at 1000 °C, the obtained ZIF-NC structure basically maintained the initial rhombic dodecahedral shape, but the size decreased to around 200 nm (Fig. 2b). This may be attributed to the loss of oxygen containing groups and volatile metal during the high temperature treatment [23]. The TEM image (Fig. 2c) of ZIF-NC further confirms that the as-prepared ZIF-NC own regular rhombic dodecahedral shape. Moreover, the TEM image of Fig. 2d indicates that the g-C₃N₄ presents layer structure. From Fig. 2e and f, distinct ZIF-NC can be clearly observed and deposited onto the surface of g-C₃N₄ with an intimate interfacial contact, which verifies the formation of the ZIF-NC/g-C₃N₄ heterostructure. The formed tight heterostructure can offer a short carrier transport distance endowing the excellent charge separation and the exposure of a large external surface area for the surface catalytic reaction.

The crystal structure of as-prepared samples was probed by X-ray diffraction patterns (XRD). As displayed in Fig. 3. The bare g-C₃N₄

shows two typical diffraction peaks at 13.2° and 27.4°, which can be assigned to the interplanar repeating structural motif (100) of tri-s-triazine units and the interlayer stacking peak (002) of aromatic systems diffraction planes, respectively [27,28]. In the case of as-prepared ZIF-NC, two broad diffraction peaks located at around 26° and 44° are assigned to the characteristic carbon (002) and (100) diffractions, respectively, indicating the presence of long-range two-dimensional ordering in the carbon matrices [22]. Meanwhile, no peaks belonged to Zn or Zn-oxide can be observed, implying that the as-prepared ZIF-NC may not contain Zn. From the XRD patterns of the ZIF-NC/g-C₃N₄ composites, only the diffraction peaks assigned to g-C₃N₄ can be observed, which may be ascribed to the low crystallinity and loading amount of ZIF-NC. Thus the ZIF-NC phase in ZIF-NC/g-C₃N₄ composites may not be clearly identified from the XRD patterns.

The FT-IR and Raman spectra of ZIF-NC/g-C₃N₄ composites are displayed and observed in Fig. 4a and b. For bare g-C₃N₄, a series of peaks located between 1200 cm^{-1} –1650 cm^{-1} are assigned to the typical stretching vibration modes of the CN heterocycles. Additionally, the peak at 811 cm^{-1} related to the s-triazine ring modes is observed [29]. In the case of ZIF-NC/g-C₃N₄ composites, the characteristic peaks corresponding to the g-C₃N₄ can be observed, indicating the existence of g-C₃N₄ phase in the composites and the introduction of ZIF-NC cannot alter the structure of g-C₃N₄. Moreover, distinct D peak at 1360 cm^{-1} and G peak at 1580 cm^{-1} can be observed in the Raman spectra of ZIF-NC, suggesting the existence of crystalline graphitic carbon in the carbonized porous carbon after high temperature treatment. The D peak is origin from in-plane imperfections, such as the defects and heteroatoms in the graphitic lattice of the disordered sp^2 -hybridized carbon, while the G peak refers to the tangential stretching mode of highly ordered pyrolytic graphite [22]. The bare g-C₃N₄ shows several sharp peaks around 500–1500 cm^{-1} which can be assigned to g-C₃N₄ [30,31]. However, it is difficult to distinguish the peak of ZIF-NC in ZIF-NC/g-C₃N₄ composites, which may be ascribed to the high intensity of fluorescence and low amount of ZIF-NC in the composite.

XPS measurements were further conducted to investigate the chemical compositions and bonding characteristics of g-C₃N₄, ZIF-NC and ZIF-NC/g-C₃N₄. As displayed in Fig. 5a, it can be observed that all samples contain only C, N and O elements without any other impurities. The absent of Zn in ZIF-NC indicates that the Zn in the parent ZIF-8 has been evaporated away at high temperatures over 1000 °C due to the low boiling point Zn atoms (melting point: 420 °C, boiling point: 907 °C) [32]. This is in accordance with the XRD result. The high resolution of N 1s spectrum of ZIF-NC (Fig. 5b) reveals the coexistence of graphitic (401.2 eV), pyrrolic (400.1 eV), and pyridinic (398.6 eV) nitrogen species, which implies that N has been successful doped into the mof-C matrix [33]. Moreover, the XPS signals of C 1s and N 1s of ZIF-NC/g-

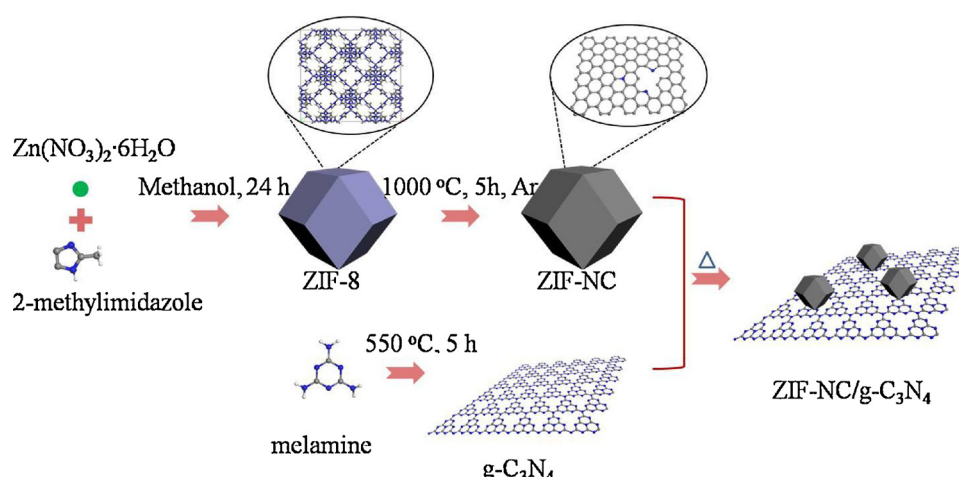


Fig. 1. Schematic illustration of the formation of ZIF-NC/g-C₃N₄ composite.

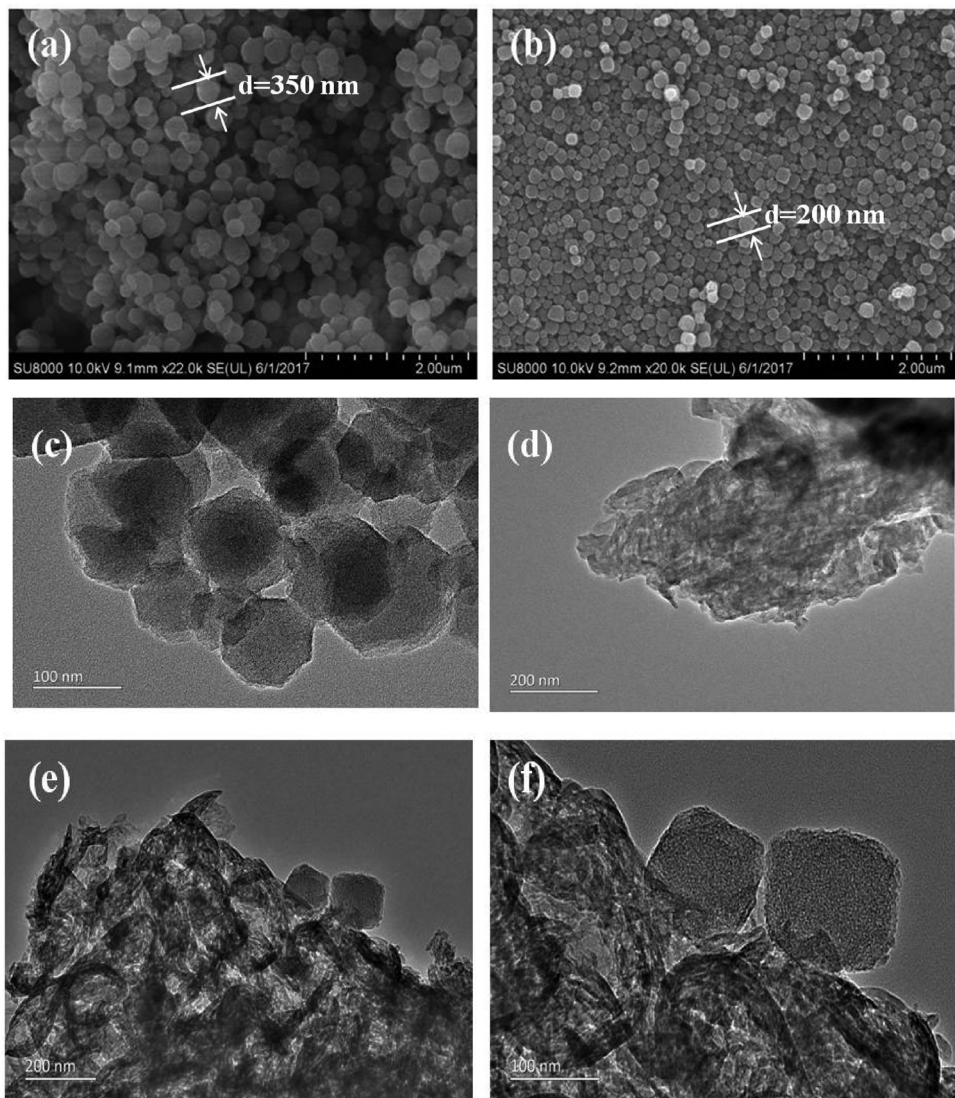


Fig. 2. SEM images of (a) ZIF-8; (b) ZIF-NC; and TEM images of (c) ZIF-NC; (d) g-C₃N₄; (e, f) ZIF-NC/g-C₃N₄.

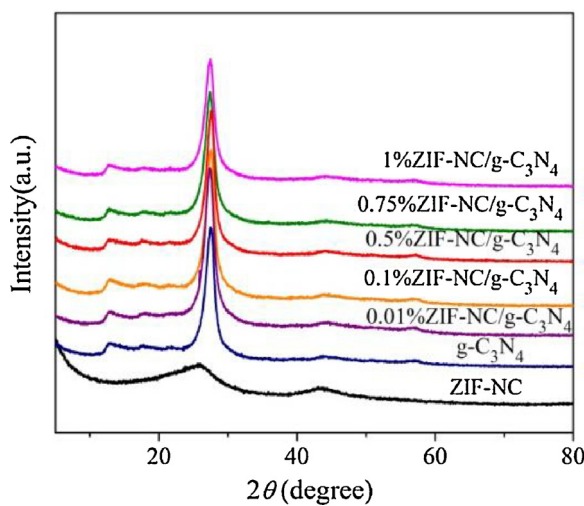


Fig. 3. XRD patterns of ZIF-NC, g-C₃N₄, and ZIF-NC/g-C₃N₄.

C₃N₄ composite are observed and shown in Fig. 5 c and d. Two peaks centered at 284.8 and 288.3 eV in C 1s XPS spectra of ZIF-NC/g-C₃N₄ composite are corresponded to contaminated carbon and sp²-bonded

carbon (N—C=N) in the g-C₃N₄. Meanwhile, the peaks at 398.4 eV and 400.5 eV ascribed to sp²-hybridized aromatic N (C—N=C) and tertiary N bonded to carbon atoms (N—C₃) of the g-C₃N₄ can be observed [27,29], further confirming the existence of g-C₃N₄ phase in the composites.

Fig. 6 shows the UV-vis diffuse reflectance spectra of the g-C₃N₄ and ZIF-NC/g-C₃N₄ composite. the bare g-C₃N₄ exhibits visible-light absorption with wavelength shorter than 450 nm which correlates with the intrinsic band gap absorption of g-C₃N₄. After ZIF-NC loading, all ZIF-NC/g-C₃N₄ composites show a high absorbance in the whole UV-vis region, especially in the visible light range, implying that the introduction of ZIF-NC into the g-C₃N₄ matrix can enhance the visible light absorption ability of g-C₃N₄. Moreover, the calculated band gaps derived from the Tauc plot (Fig. 6b) of the g-C₃N₄ and ZIF-NC/g-C₃N₄ composite were estimated to be 2.65 eV and 2.35 eV, respectively, also indicating that the introduction of ZIF-NC can narrow the bandgap of g-C₃N₄.

3.2. Photocatalytic activity

The photocatalytic activities toward BPA degradation over the g-C₃N₄ and ZIF-NC/g-C₃N₄ composites with PMS were evaluated under visible light irradiation ($\lambda > 400$ nm). As depicted in Fig. 7, the blank

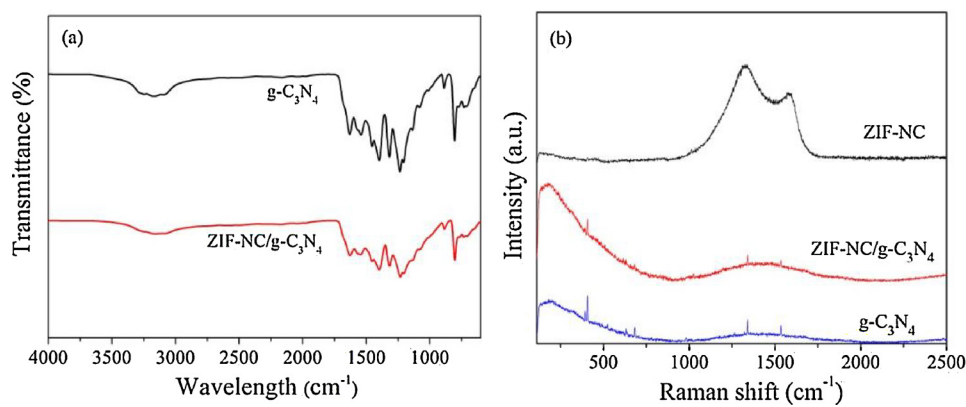


Fig. 4. (a) FTIR spectra and (b) Raman spectra of ZIF-NC, g-C₃N₄ and ZIF-NC/g-C₃N₄.

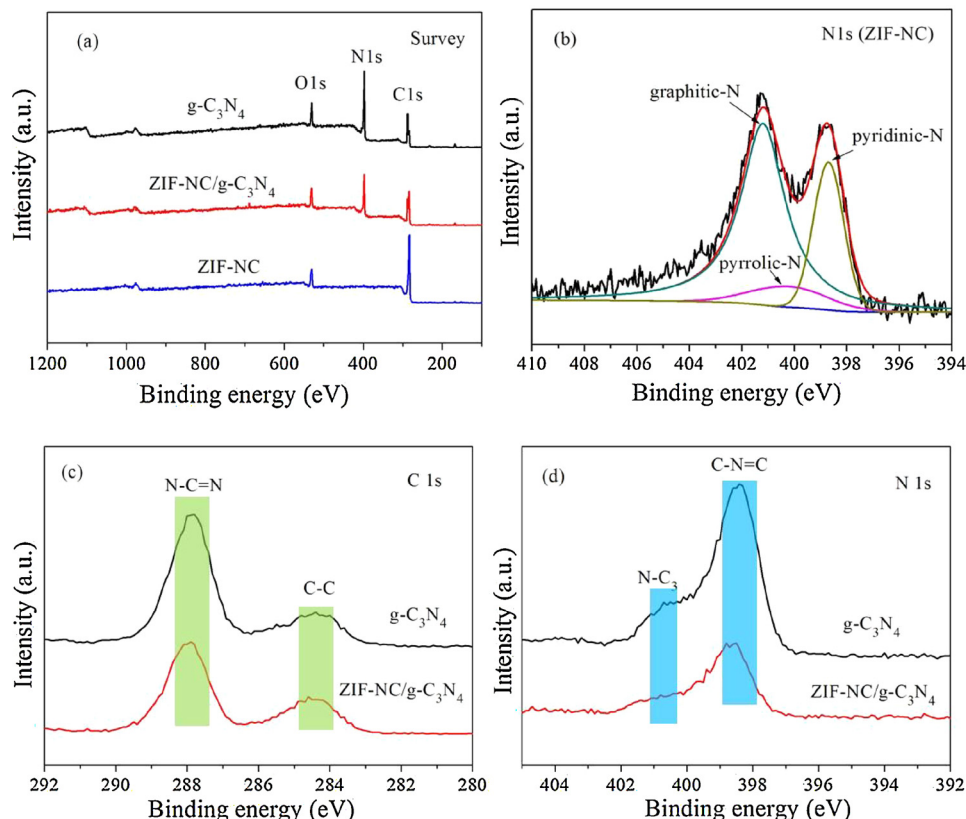


Fig. 5. (a) XPS survey spectrums of g-C₃N₄, ZIF-NC and ZIF-NC/g-C₃N₄; (b) the high-resolution N 1s of ZIF-NC; (c, d) the C 1s and N 1s of the g-C₃N₄ and ZIF-NC/g-C₃N₄.

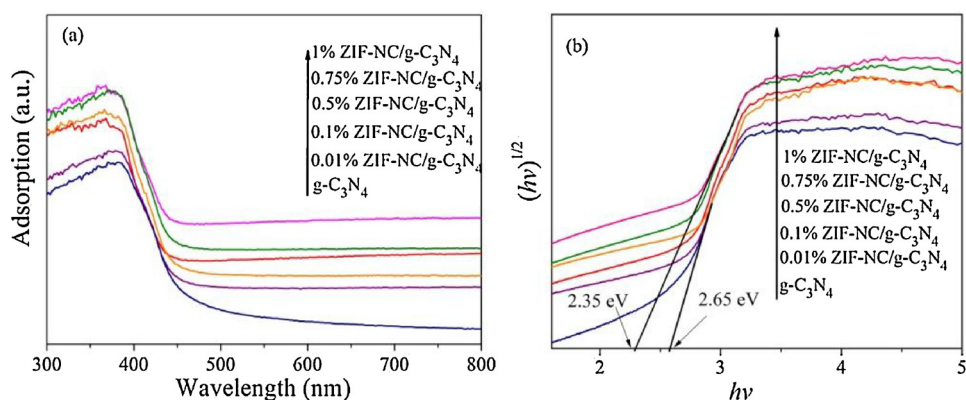


Fig. 6. (a) UV-vis diffuse reflectance spectra of g-C₃N₄ and ZIF-NC/g-C₃N₄ photocatalysts and (b) the corresponding Tauc plot.

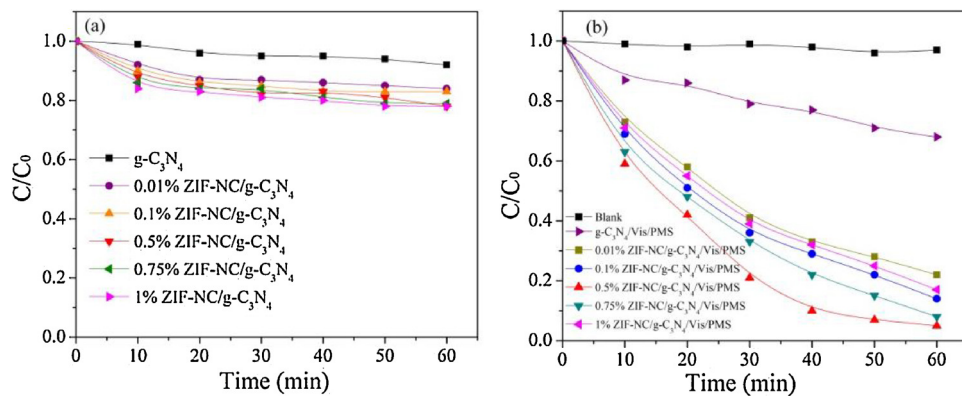


Fig. 7. (a) The adsorption of BPA over $g\text{-C}_3\text{N}_4$ and ZIF-NC/g-C₃N₄ samples in the dark; (b) Photocatalytic activities of BPA degradation over ZIF-NC/g-C₃N₄ with different content of ZIF-NC under visible light irradiation.

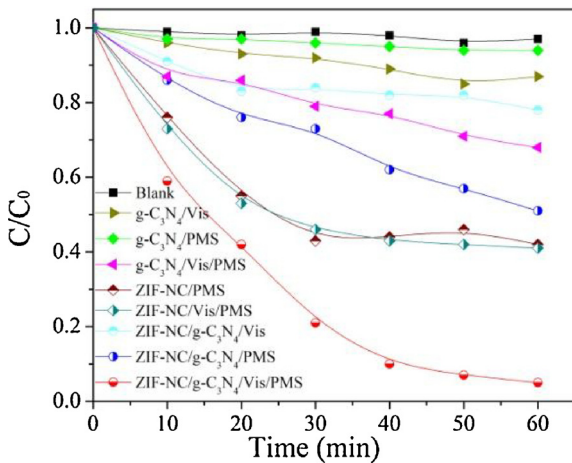


Fig. 8. Photocatalytic activities of BPA degradation over $g\text{-C}_3\text{N}_4$, ZIF-NC and ZIF-NC/g-C₃N₄ samples under visible light irradiation.

experiment (without catalyst and PMS) demonstrates that BPA show negligible photodecomposition under visible light irradiation. Prior to reaction, the adsorption experiments performed in the dark (Fig. 7a) reveals that all ZIF-NC/g-C₃N₄ composites possess higher adsorption capability toward BPA in compared with the $g\text{-C}_3\text{N}_4$. This may be ascribed to the unique nanoporous structure of ZIF-NC with large specific surface area, which facilitates the adsorption of BPA. Under visible light irradiation, the ZIF-NC/g-C₃N₄ composites with PMS exhibit remarkably enhanced photocatalytic activity as compared to the $g\text{-C}_3\text{N}_4$ under the same experimental conditions (Fig. 7b). In particular, the 0.5%ZIF-NC/g-C₃N₄ composite with PMS exhibits the superior

photocatalytic activity with removal rate of 97% after 60 min irradiation. It is also worthy of notice that the content of ZIF-NC in the composites has a great influence on the photocatalytic activity of the samples. As the content of ZIF-NC increased from 0.01% to 0.5%, the photocatalytic activities of the hybrids improve gradually and the 0.5% ZIF-NC/g-C₃N₄ composite shows the highest photocatalytic activity. However, the photocatalytic activity decreased with further increasing the proportion of ZIF-NC content from 0.5% to 1%. This can be explained by the fact that the excessive ZIF-NC loaded on the $g\text{-C}_3\text{N}_4$ hinder the light adsorption of $g\text{-C}_3\text{N}_4$, results in less photogenerated electron-hole pairs in the $g\text{-C}_3\text{N}_4$ could participate in reactions. In order to explore the role of ZIF-NC in this reaction, the photocatalytic activities of different $g\text{-C}_3\text{N}_4$, ZIF-NC and ZIF-NC/g-C₃N₄ systems for BPA degradation were also assessed. As depicted in Fig. 8, the ZIF-NC/g-C₃N₄ systems exhibit enhanced photocatalytic activities in compared with the $g\text{-C}_3\text{N}_4$ and ZIF-NC counterparts, indicating that the introduction of ZIF-NC can indeed improve the photocatalytic performance of $g\text{-C}_3\text{N}_4$. Especially, the addition of PMS can further improve the photocatalytic performance of the ZIF-NC/g-C₃N₄ systems. Because of the excellent activity of ZIF-NC for PMS activation, the ZIF-NC/PMS and ZIF-NC/Vis/PMS system show certain activities for BPA degradation. However, the visible-light shows negligible effect on these two systems, which may be ascribed to the no light-response ability of ZIFNC. Moreover, the activities of ZIF-NC/PMS and ZIFNC/Vis/PMS system are lower than that of the corresponding ZIF-NC/g-C₃N₄ system, further indicating the outstanding photocatalytic activity of ZIF-NC/g-C₃N₄/Vis/PMS system for BPA degradation. The reaction kinetics of the degradation of BPA over $g\text{-C}_3\text{N}_4$ and ZIF-NC/g-C₃N₄ composites were investigated and illustrated in Fig. 9. The linear relationship suggests that the reaction follows pseudo-first-order kinetics and the apparent rate constant k for the BPA degradation over 0.5% ZIF-NC/g-C₃N₄/Vis/PMS system is

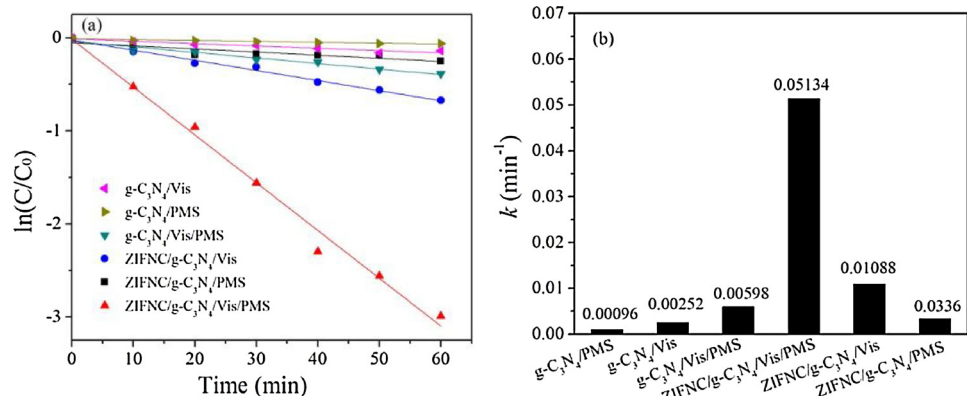


Fig. 9. (a) Comparison of kinetic constants of BPA degradation with different systems; (b) the calculated corresponding k of different systems.

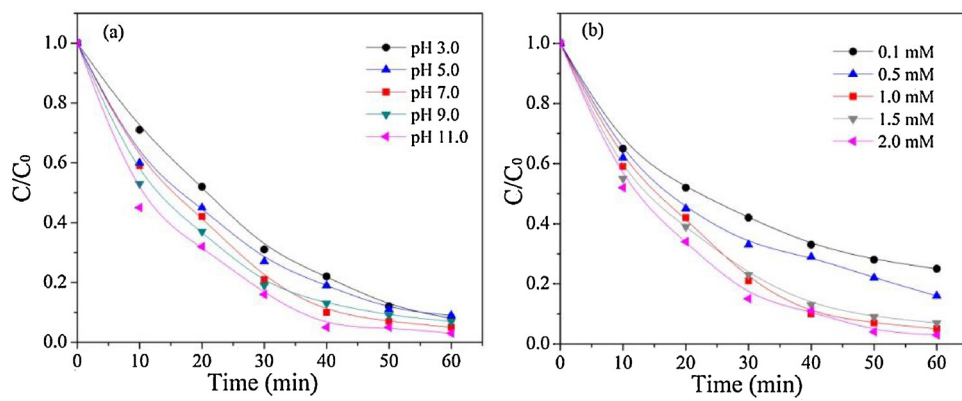


Fig. 10. Influence of (a) initial pH values and (b) PMS concentration on the removal efficiency of BPA.

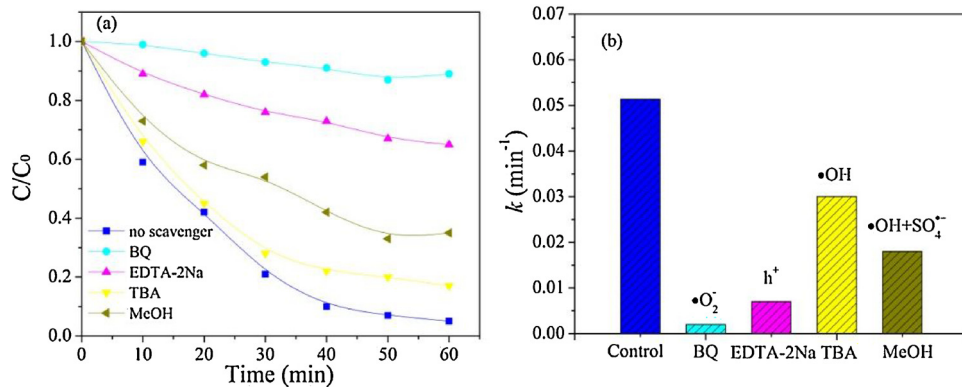


Fig. 11. (a) Reactive species trapping experiments of ZIF-NC/g-C₃N₄ with PMS under visible light irradiation; (b) the corresponding reaction constants.

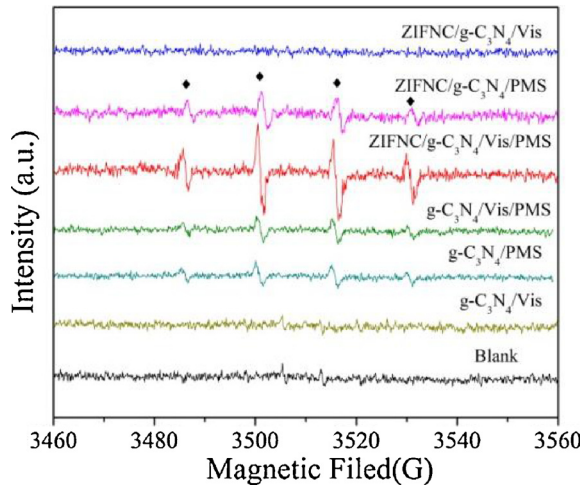


Fig. 12. ESR signals in various photocatalysts system.

0.05134 min^{-1} , which is almost 8.6 times as high as that of g-C₃N₄/Vis/PMS system (0.00598 min^{-1}). In addition, the constant k of 0.5% ZIF-NC/g-C₃N₄/Vis/PMS system is also 4.7 times as that of 0.5% ZIF-NC/g-C₃N₄/Vis system (0.01088 min^{-1}), further suggesting that the introduction of PMS can dramatically improve the photocatalytic activity of ZIF-NC/g-C₃N₄. This may be ascribed to the enhanced PMS activation for $\text{SO}_4^{\cdot-}$ production by the ZIF-NC.

The impacts of initial pH and PMS concentration on the degradation of BPA by ZIF-NC/g-C₃N₄ system were also investigated. As illustrated in Fig. 10a, The ZIF-NC/g-C₃N₄ system shows effective photocatalytic activity toward BPA degradation over a broad initial pH range, and the removal efficiency of BPA is accelerated with the increase of the initial

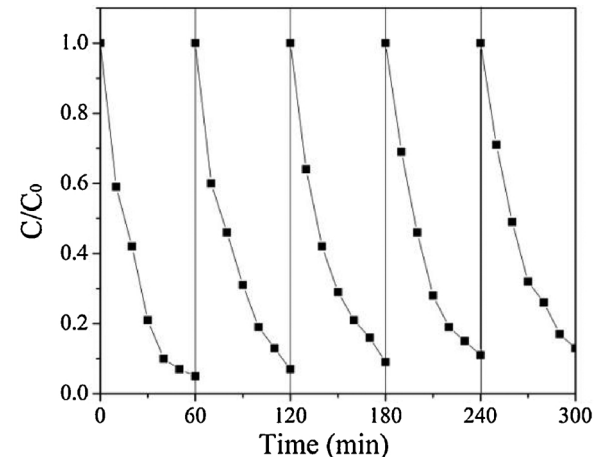


Fig. 13. Cycling test of ZIF-NC/g-C₃N₄ for BPA removal.

pH. It has been reported that the H_2SO_5 is the major form of PMS when the pH value is lower than that of the pKa of PMS ($\text{pKa} = 9.4$) [9,11]. Because of the formed H_2SO_5 is stable under acid condition, the activation of PMS can be inhibited under relatively low pH value. On the contrary, the BPA degradation rate with initial pH 11.0 is higher than others, which is due to the pH decreases slower than others [9,34]. In addition, the influence of PMS concentration on the degradation of BPA has been studied and shown in Fig. 10b. Apparently, the degradation efficiency of BPA improved gradually when the PMS concentration increased from 0.1 to 1.0 mM. However, only a slight increase for the removal of BPA is observed when the PMS concentration further increased to 2.0 mM. This can be explained by the self-quenching reaction between the produced $\text{SO}_4^{\cdot-}$ and the excess PMS [22].

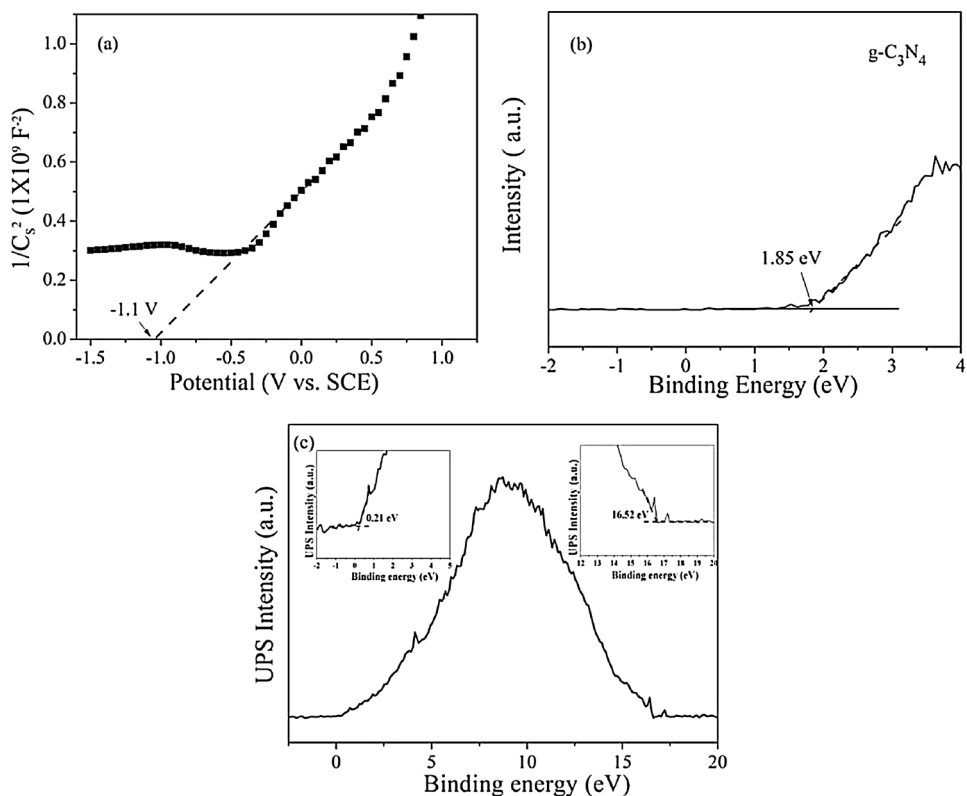


Fig. 14. (a) Mott-Schottky plots and (b) VB-XPS spectra of $g\text{-C}_3\text{N}_4$; (c) the UPS spectra of ZIF-NC.

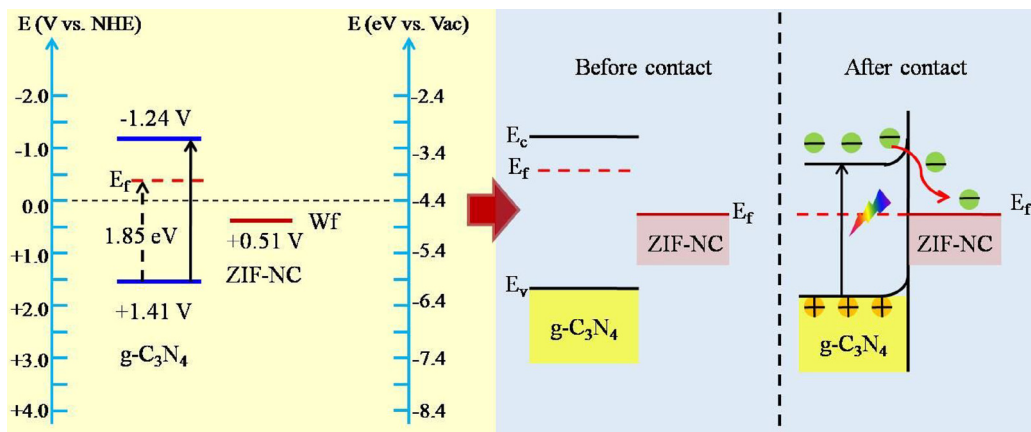


Fig. 15. Schematic diagram of band structure and charge transfer between $g\text{-C}_3\text{N}_4$ and ZIF-NC.

To clarify the contribution of different active radicals in the photocatalytic reaction of ZIF-NC/ $g\text{-C}_3\text{N}_4$ composite, radical trapping experiments were performed. In this study, the scavengers EDTA-2Na and BQ were employed to capture the photogenerated hole (h^+) and superoxide anion radicals ($\cdot\text{O}_2^-$) species in the photocatalytic processes, respectively. The methanol (MeOH) was used as hydroxyl radicals ($\cdot\text{OH}$) and sulfate radicals ($\text{SO}_4\cdot^-$) scavenger because of the similar reactivity toward $\cdot\text{OH}$ ($K = 9.7 \times 10^8 \text{ M}^{-1}\text{s}^{-1}$) and $\text{SO}_4\cdot^-$ ($K = 2.5 \times 10^7 \text{ M}^{-1}\text{s}^{-1}$) [16,34], whereas the TBA, a alcohol lacking α -hydrogen, was used to scavenge the $\cdot\text{OH}$ ($K = 3.8\text{--}7.6 \times 10^8 \text{ M}^{-1}\text{s}^{-1}$) instead of $\text{SO}_4\cdot^-$ ($K = 4.0\text{--}9.1 \times 10^5 \text{ M}^{-1}\text{s}^{-1}$) [16,35]. The methanol and TBA can be used to differentiate $\text{SO}_4\cdot^-$ from $\cdot\text{OH}$. The influence of adding different scavengers toward the degradation efficiency of BPA are illustrated in Fig. 11a and b. It can be clearly seen that all scavengers show inhibited effect in the degradation efficiency of BPA. Notably, the degradation efficiency of BPA decreases markedly

after addition of BQ and EDTA-2Na into the system, which demonstrated that $\cdot\text{O}_2^-$ radicals and h^+ are the predominant active species in the photocatalytic reaction. Meanwhile, the introduction of MeOH and TBA into the photocatalytic system can also decrease the photocatalytic degradation efficiency of BPA, suggesting that the $\text{SO}_4\cdot^-$ and $\cdot\text{OH}$ are responsible in the photocatalytic process. Specifically, the MeOH show higher inhibition performance than that of TBA, indicating that the $\text{SO}_4\cdot^-$ show obviously responsible for the BPA degradation.

In order to further confirm the active radicals in ZIF-NC/ $g\text{-C}_3\text{N}_4$ /Vis/PMS system, ESR technique was employed to detect the active radicals in the photocatalytic reaction systems. As depicted in Fig. 12, the results reveal that no DMPO- $\cdot\text{OH}$ or DMPO- $\text{SO}_4\cdot^-$ signals can be observed under blank condition, which indicates that these radicals are generated only in the presence of photocatalysts. As expected, a distant DMPO- $\cdot\text{OH}$ signal, as verified by four-line ESR signals with the relative intensities of 1:2:2:1, can be observed in ZIF-NC/ $g\text{-C}_3\text{N}_4$ /Vis/PMS and

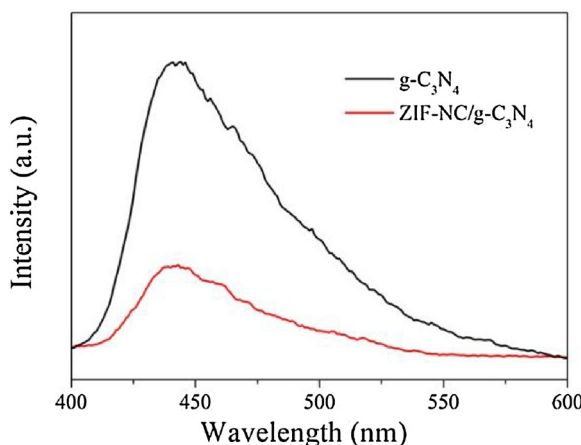


Fig. 16. PL spectra of $\text{g-C}_3\text{N}_4$ and ZIF-NC/g-C₃N₄.

ZIF-NC/g-C₃N₄/PMS. These $\cdot\text{OH}$ radicals are produced by the reaction between $\text{SO}_4^{\cdot-}$ and $\text{H}_2\text{O}/\text{OH}^-$ [9,36], whereas there is no $\cdot\text{OH}$ signal in ZIF-NC/g-C₃N₄/Vis system. This result indicates that ZIF-NC can be used as an efficient catalyst for PMS activation to yield $\text{SO}_4^{\cdot-}$ radicals. In compared, $\text{g-C}_3\text{N}_4$ /Vis/PMS, $\text{g-C}_3\text{N}_4$ /Vis and $\text{g-C}_3\text{N}_4$ /PMS system were tested. No obvious DMPO- $\cdot\text{OH}$ signal can be detected in $\text{g-C}_3\text{N}_4$ /Vis system which may be ascribed to weak oxidation of photogenerated holes of $\text{g-C}_3\text{N}_4$. In contrast, an obvious $\cdot\text{OH}$ signal can be observed in the $\text{g-C}_3\text{N}_4$ /Vis/PMS and $\text{g-C}_3\text{N}_4$ /PMS system. However, the relative intensities of these two systems are lower than that of ZIF-NC modified $\text{g-C}_3\text{N}_4$ system, implying the less active sites of $\text{g-C}_3\text{N}_4$ for PMS activation. Base on the above results, it is clearly indicated that the introduction of ZIF-NC can enhance the activation of PMS for $\text{SO}_4^{\cdot-}$ radicals production.

Moreover, the durability of the ZIF-NC/g-C₃N₄ composite was further evaluated by five consecutive operations. As shown in Fig. 13, only a slightly decrease (~8%) of the photocatalytic activity for BPA degradation can be observed after five runs, suggesting the robust photocatalytic stability of ZIF-NC/g-C₃N₄ composites.

3.3. Mechanism of photocatalytic activity enhancement

The above results clearly reveal that the photocatalytic activity of g-C₃N₄ can be improved by integration of ZIF-NC with g-C₃N₄ to form heterostructure. The band alignment between g-C₃N₄ and ZIF-NC leading to the formation of heterostructure is supposed to play a key role in enhancing the photocatalytic activity of ZIF-NC/g-C₃N₄. To explore the relative band position of the g-C₃N₄ and ZIF-NC, Mott-Schottky measurement, valence band X-ray photoelectron spectroscopy (VB-XPS) and ultraviolet photoelectron spectroscopy (UPS) were

conducted. The band edge position of g-C₃N₄ can be evaluated through the Mott-Schottky measurement, VB-XPS and UV/Vis spectra [37]. As shown in Fig. 14a, the flat-band position g-C₃N₄ obtained from the Mott-Schottky plot is -1.1 V versus saturated calomel electrode (SCE), which corresponded to -0.44 V versus the normal hydrogen electrode (NHE). The positive slope of the epitaxial tangent of the plot indicates the n-type features of g-C₃N₄. Previous studies reported that the flat-band potential of n-type semiconductor equals the Fermi level [37,38]. Thus the Fermi level of g-C₃N₄ can be determined to be -0.44 V (NHE). The VB-XPS result (Fig. 14b) reveals that the energy gap between the VB and the Fermi level (E_F) is 1.85 eV for g-C₃N₄. So, the valence band edge potential of g-C₃N₄ can be calculated to be 1.41 V. Since the band gaps (E_g) value of g-C₃N₄ is 2.65 eV (Fig. 6b), the CB band edge potential of g-C₃N₄ can be estimated to be -1.24 V. In view of the intrinsic high conductive feature of ZIF-NC, ultraviolet photoelectron spectroscopy (UPS) was conducted to determine the work function of ZIF-NC. The onset (E_i) and cutoff (E_{cutoff}) energy was 0.21 and 16.52 eV, respectively, as shown in Fig. 14c. Thus, the work function of ZIF-NC was calculated to be -4.91 eV by subtracting the width of the UPS spectra from the excitation energy (21.22 eV), which can be converted to $+0.51$ V in Volts. As illustrated in Fig. 15, apparently, the Fermi level of g-C₃N₄ is more negative than that of the ZIF-NC. According to energy band theory, when both g-C₃N₄ and ZIF-NC are integrated together to form a heterojunction, the difference between the Fermi levels of g-C₃N₄ and ZIF-NC causes the electrons in g-C₃N₄ to flow into ZIF-NC at the interface until the Fermi levels of the two components in the heterostructure are equal. As evidenced by the Raman result, a typical D peak and G peak can be observed in ZIF-NC, demonstrating the existence of crystalline graphitic carbon in the carbonized porous carbon. As we know, the crystalline graphitic carbon shows excellent electrical conductivity which is comparable to the metal [39,40]. Thus a Schottky junction can be formed at the interface of g-C₃N₄ and ZIF-NC. The photoinduced electrons of g-C₃N₄ can move rapidly across the interface and fasten to the surface of ZIF-NC, results in the accelerate photo-generated charge separation.

To validate the aforementioned charge transfer mechanism, the steady-state PL spectra were recorded and shown in Fig. 16. The emission peak of ZIF-NC/g-C₃N₄ is significantly weakened in comparison with that of bare g-C₃N₄, indicating the greatly suppressed charge recombination and boosted interfacial charge transfer. Meanwhile, to probe the specific charge carrier dynamics of the g-C₃N₄ and ZIF-NC/g-C₃N₄, the time-resolved photoluminescence spectra were recorded and displayed in Fig. 17. The plots on a semilog scale revealed that the dynamics of the samples follow second order exponential decay behavior and the emission decay curves were fitted by a double-exponential model with low uncertainties (χ) in which two decay components are derived (insets in Fig. 17a and b). Obviously, the average emission lifetime of ZIF-NC/g-C₃N₄ (2.73 ns) was shorter than that of the

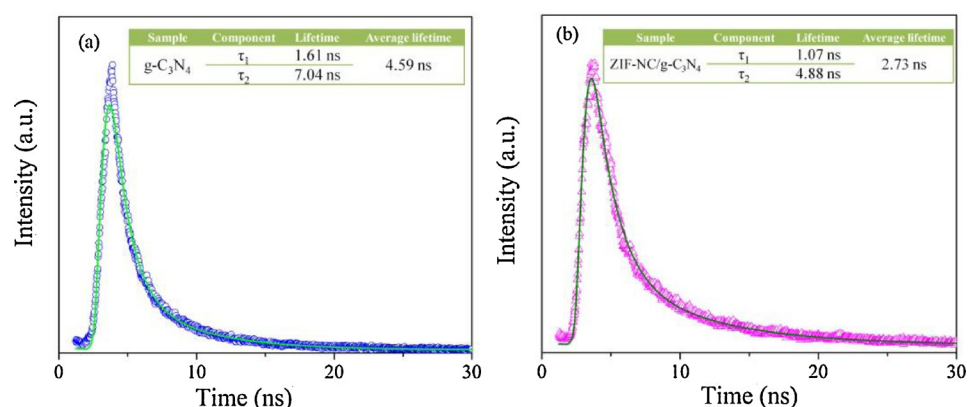


Fig. 17. Time-resolved transient PL decay of (a) g-C₃N₄ and (b) ZIF-NC/g-C₃N₄.

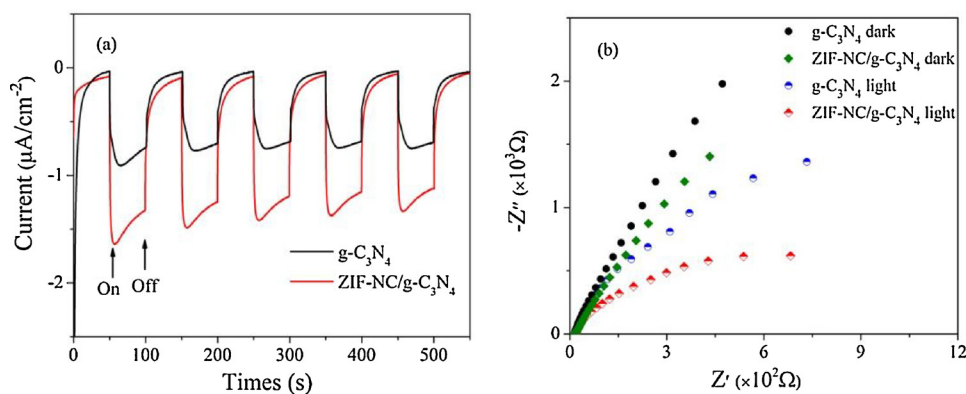


Fig. 18. (a) Transient photocurrent density responses of $g\text{-C}_3\text{N}_4$ and ZIF-NC/ $g\text{-C}_3\text{N}_4$ sample electrodes with light on/off cycles under visible light irradiation; (b) EIS Nyquist plots of the $g\text{-C}_3\text{N}_4$ and ZIF-NC/ $g\text{-C}_3\text{N}_4$.

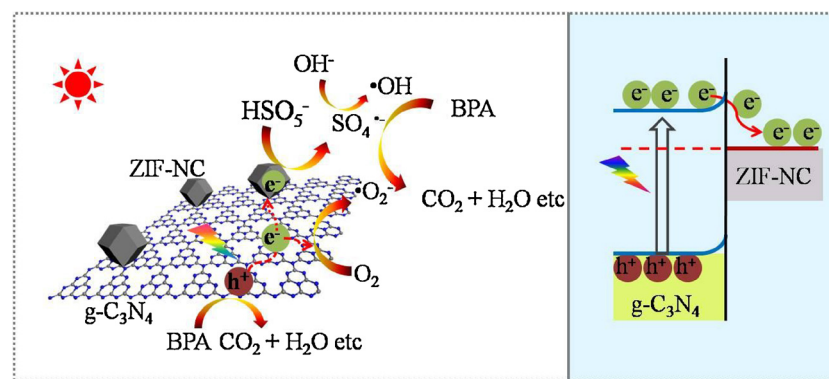


Fig. 19. Proposed photocatalytic mechanism of ZIF-NC/ $g\text{-C}_3\text{N}_4$.

corresponding bulk $g\text{-C}_3\text{N}_4$ counterpart (4.59 ns). This decreased carrier lifetime suggested significantly accelerated photoexciton dissociation in the ZIF-NC/ $g\text{-C}_3\text{N}_4$ sample through non-radiative quenching pathway [41–44], confirming the proposed spatially separated photocarriers at the interface between $g\text{-C}_3\text{N}_4$ and ZIF-NC. In addition, the related electron-transfer rate constant (k_{et}) in ZIF-NC/ $g\text{-C}_3\text{N}_4$ is calculated to be $1.48 \times 10^8 \text{ S}^{-1}$ using the following Eq. (1) [31,38]:

$$ket(g - \text{C}_3\text{N}_4 \rightarrow \text{ZIF-NC}/g - \text{C}_3\text{N}_4) = \frac{1}{< \tau > (\text{ZIF-NC}/g - \text{C}_3\text{N}_4)} - \frac{1}{< \tau > (g - \text{C}_3\text{N}_4)} \quad (1)$$

The corresponding observations of PL quenching and lifetime reduction suggest the establishment of an electron transfer channel from $g\text{-C}_3\text{N}_4$ to ZIF-NC in a non-radiative quenching pathway, which is coincided with the above band alignment analysis. Accordingly, this leads to efficient interfacial charge transfer and minimize the recombination of photoexcited charge in the ZIF-NC/ $g\text{-C}_3\text{N}_4$ hybrid.

Furthermore, as shown in Fig. 18a, the photo-chronoamperometry measurements also support the above conclusion. The photogenerated current density of the ZIF-NC/ $g\text{-C}_3\text{N}_4$ displays ca. 2.1-fold photocurrent enhancement over bulk $g\text{-C}_3\text{N}_4$ under the same experimental condition. The significantly enhanced transient photogenerated current of ZIF-NC/ $g\text{-C}_3\text{N}_4$ indicates that the electron-hole pairs generated in the ZIF-NC/ $g\text{-C}_3\text{N}_4$ composite can be separated more efficiently than those of bulk $g\text{-C}_3\text{N}_4$. In addition, the electrochemical impedance spectrum of ZIF-NC/ $g\text{-C}_3\text{N}_4$ (Fig. 18b) shows a smaller semicircular in the Nyquist plot than that of bare $g\text{-C}_3\text{N}_4$, indicating a lower charge-transfer resistance in the hybrid composite, which warrants efficient transportation and separation of charge carriers in ZIF-NC/ $g\text{-C}_3\text{N}_4$. Collectively, these commendable photo- and electrochemical measurements support that the introduction of ZIF-NC in $g\text{-C}_3\text{N}_4$ is highly efficient in promoting

electron–hole pair separation and accelerating the surface reaction rate of the ZIF-NC/ $g\text{-C}_3\text{N}_4$ composites.

On the basis of the above discussion, a tentative mechanism for the photocatalytic BPA degradation over the ZIF-NC/ $g\text{-C}_3\text{N}_4$ composite with PMS is proposed, as illustrated in Fig. 19. Upon visible light irradiation, electrons are promoted from the valence band of $g\text{-C}_3\text{N}_4$ to its corresponding conduction band. On one hand, the photogenerated electrons can cross the interface between $g\text{-C}_3\text{N}_4$ and ZIF-NC, and fasten to the surface of ZIF-NC to react with the adsorbed PMS to yield $\text{SO}_4^{\cdot-}$ radicals. On the other hand, the electrons can migrate to the surface of $g\text{-C}_3\text{N}_4$ to reduce the adsorbed O_2 for $\cdot\text{O}_2^-$ radicals production. The formed active radicals can decompose the BPA rapidly, and simultaneously, the holes that remained within the valence band of $g\text{-C}_3\text{N}_4$ can directly react with BPA. As a result, the ZIF-NC/ $g\text{-C}_3\text{N}_4$ composite exhibited remarkable photocatalytic performance toward BPA degradation with PMS.

4. Conclusion

In summary, we report the fabrication of heterostructure ZIF-NC/ $g\text{-C}_3\text{N}_4$ composite via a facile thermal treatment method. The as-prepared composite manifests obvious enhanced photocatalytic activity toward BPA degradation with PMS as compared with $g\text{-C}_3\text{N}_4$. The apparent rate constant k for BPA degradation over the ZIF-NC/ $g\text{-C}_3\text{N}_4$ sample with PMS is 0.05134 min^{-1} , which is about 8.4 times as high as that of $g\text{-C}_3\text{N}_4$. This improved photocatalytic activity can be attributed to enhanced light harvesting and efficient interfacial charge separation between $g\text{-C}_3\text{N}_4$ and ZIF-NC as well as abundant surface active sites for PMS activation to $\text{SO}_4^{\cdot-}$ production for BPA removal. This work will provide a strategy to design other novel composite with enhanced photocatalytic performance in environmental remediation.

Acknowledgements

This work was financially supported by the National Natural Science Foundation of China (21777106); the National Major Science and Technology Program for Water Pollution Control and Treatment (2017ZX07202); and the Science and Technology Innovation Commission of Shenzhen (grant number JCYJ20170302141241005).

References

- [1] X.C. Wang, K. Maeda, A. Thomas, K. Takanabe, G. Xin, J.M. Carlsson, K. Domen, M. Antonietti, Polymer semiconductors for artificial photosynthesis: hydrogen evolution by mesoporous graphitic carbon nitride with visible light, *Nat. Mater.* 8 (2009) 76–80.
- [2] Y. Wang, X.C. Wang, M. Antonietti, Polymeric graphitic carbon nitride as a heterogeneous organocatalyst: from photochemistry to multipurpose catalysis to sustainable chemistry, *Angew. Chem. Int. Ed.* 51 (2012) 68–89.
- [3] G.P. Dong, Y.H. Zhang, Q.W. Pan, J.R. Qiu, A fantastic graphitic carbon nitride ($g\text{-C}_3\text{N}_4$) material: Electronic structure, photocatalytic and photoelectronic properties, *J. Photochem. Photobiol. C: Photocom. Rev.* 20 (2014) 33–50.
- [4] J.J. Zhu, P. Xiao, H.L. Li, S.A.C. Carabineiro, graphitic carbon nitride: synthesis, properties, and applications in catalysis, *ACS Appl. Mater. Interfaces* 6 (2014) 16449–16465.
- [5] X.C. Wang, S. Blechert, M. Antonietti, Polymeric graphitic carbon nitride for heterogeneous photocatalysis, *ACS Catal.* 2 (2012) 1596–1606.
- [6] M.Y. Wei, L. Gao, J. Li, J. Fang, W.X. Cai, X.X. Li, A.H. Xu, Activation of peroxymonosulfate by graphitic carbon nitride loaded on activated carbon for organic pollutants degradation, *J. Hazard. Mater.* 316 (2016) 60–68.
- [7] F. Wu, H.W. Huang, T.F. Xu, W.Y. Lu, N. Li, W.X. Chen, Visible-light-assisted peroxymonosulfate activation and mechanism for the degradation of pharmaceuticals over pyridyl-functionalized graphitic carbon nitride coordinated with iron phthalocyanine, *Appl. Catal. B* 218 (2017) 230–239.
- [8] Y.F. Tao, Q. Ni, M.Y. Wei, D.S. Xia, X.X. Li, A.H. Xu, Metal-free activation of peroxymonosulfate by $g\text{-C}_3\text{N}_4$ under visible light irradiation for the degradation of organic dyes, *RSC Adv.* 5 (2015) 44128–44136.
- [9] Y.B. Wang, X. Zhao, D. Cao, Y. Wang, Y.F. Zhu, Peroxymonosulfate enhanced visible light photocatalytic degradation bisphenol A by single-atom dispersed Ag mesoporous $g\text{-C}_3\text{N}_4$ hybrid, *Appl. Catal. B* 211 (2017) 79–88.
- [10] H.J. Dong, M.Y. Wei, J. Li, J. Fang, L. Gao, X.X. Li, A.H. Xu, Catalytic performance of supported $g\text{-C}_3\text{N}_4$ on MCM-41 in organic dye degradation with peroxymonosulfate, *RSC Adv.* 6 (2016) 70747–70755.
- [11] B.C. Liu, M. Qiao, Y.B. Wang, L.J. Wang, Y. Gong, T. Guo, X. Zhao, Persulfate enhanced photocatalytic degradation of bisphenol A by $g\text{-C}_3\text{N}_4$ nanosheets under visible light irradiation, *Chemosphere* 189 (2017) 115–122.
- [12] H.X. Shao, X. Zhao, Y.B. Wang, R. Mao, Y. Wang, M. Qiao, S. Zhao, Y.F. Zhu, Synergistic activation of peroxymonosulfate by Co_3O_4 modified $g\text{-C}_3\text{N}_4$ for enhanced degradation of diclofenac sodium under visible light irradiation, *Appl. Catal. B* 218 (2017) 810–818.
- [13] F. Ghanbari, M. Moradi, Application of peroxymonosulfate and its activation methods for degradation of environmental organic pollutants: review, *Chem. Eng. J.* 310 (2017) 41–62.
- [14] H.B. Zeng, S.S. Liu, B.Y. Chai, D. Cao, Y. Wang, X. Zhao, Enhanced photoelectrocatalytic decomplexation of Cu-EDTA and Cu recovery by persulfate activated by UV and cathodic reduction, *Environ. Sci. Technol.* 50 (2016) 6459–6466.
- [15] M.G. Antoniou, A.A. Delacruz, D.D. Dionysiou, Intermediates and reaction pathways from the degradation of microcystin-LR with sulfate radicals, *Environ. Sci. Technol.* 44 (2010) 7238–7244.
- [16] T. Zeng, X.L. Zhang, S.H. Wang, H.Y. Niu, Y.Q. Cai, Spatial confinement of a Co_3O_4 catalyst in hollow metal-organic frameworks as a nanoreactor for improved degradation of organic pollutants, *Environ. Sci. Technol.* 49 (2015) 2350–2357.
- [17] A. Farhat, J. Keller, S. Tait, J. Radjenovic, Removal of persistent organic contaminants by electrochemically activated sulfate, *Environ. Sci. Technol.* 49 (2015) 14326–14333.
- [18] H.Q. Sun, S.Z. Liu, G.L. Zhou, H.M. Ang, M.O. Tadé, S.B. Wang, Reduced graphene oxide for catalytic oxidation of aqueous organic pollutants, *ACS Appl. Mater. Interfaces* 10 (2012) 5466–5471.
- [19] X.G. Duan, H.Q. Sun, Y.X. Wang, J. Kang, S.B. Wang, N-doping-induced nonradical reaction on single-walled carbon nanotubes for catalytic phenol oxidation, *ACS Catal.* 5 (2015) 553–559.
- [20] S. Indrawirawan, H.Q. Sun, X.G. Duan, S.B. Wang, Nanocarbons in different structural dimensions (0–3D) for phenol adsorption and metal-free catalytic oxidation, *Appl. Catal. B* 179 (2015) 352–362.
- [21] X.K. Kong, C.L. Chen, Q.W. Chen, Doped graphene for metal-free catalysis, *Chem. Soc. Rev.* 43 (2014) 2841–2857.
- [22] G.L. Wang, S. Chen, X. Quan, H.T. Yu, Y.B. Zhang, Enhanced activation of peroxymonosulfate by nitrogen doped porous carbon for effective removal of organic pollutants, *Carbohydr. Res.* 115 (2017) 730–739.
- [23] Q.J. Xiang, J.G. Yu, M. Jaroniec, Preparation and enhanced visible-light photocatalytic H_2 -production activity of graphene/ C_3N_4 composites, *J. Phys. Chem. C* 115 (2011) 7355–7363.
- [24] X.J. Bai, L. Wang, Y.J. Wang, W.Q. Yao, Y.F. Zhu, Enhanced oxidation ability of $g\text{-C}_3\text{N}_4$ photocatalyst via C_{60} modification, *Appl. Catal. B* 152–153 (2014) 262–270.
- [25] Y.G. Xu, H. Xu, L. Wang, J. Yan, H.M. Li, Y.H. Song, L.Y. Huang, G.B. Cai, The CNT modified white C_3N_4 composite photocatalyst with enhanced visible-light response photoactivity, *Dalton Trans.* 42 (2013) 7604–7613.
- [26] G.Z. Liao, S. Chen, X. Quan, H.T. Yu, H.M. Zhao, Graphene oxide modified $g\text{-C}_3\text{N}_4$ hybrid with enhanced photocatalytic capability under visible light irradiation, *J. Mater. Chem.* 22 (2012) 2721–2726.
- [27] Y.M. He, L.H. Zhang, B.T. Teng, M.H. Fan, New application of Z-scheme $\text{Ag}_3\text{PO}_4/g\text{-C}_3\text{N}_4$ composite in converting CO_2 to fuel, *Environ. Sci. Technol.* 49 (2015) 649–656.
- [28] J.C. Wang, H.C. Yao, Z.Y. Fan, L. Zhang, J.S. Wang, S.Q. Zang, Z.J. Li, Indirect Z-scheme $\text{BiOI}/g\text{-C}_3\text{N}_4$ photocatalysts with enhanced photoreduction CO_2 activity under visible light irradiation, *ACS Appl. Mater. Interfaces* 8 (2016) 3765–3775.
- [29] D.M. Chen, K.W. Wang, W.Z. Hong, R.L. Zong, W.Q. Yao, Y. F. Zhu, Visible light photoactivity enhancement via CuTCPI hybridized $g\text{-C}_3\text{N}_4$ nanocomposite, *Appl. Catal. B* 166–167 (2015) 366–373.
- [30] Y. Shiraishi, S. Kanazawa, Y. Kofuji, H. Sakamoto, S. Ichikawa, S. Tanaka, T. Hirai, Sunlight-driven hydrogen peroxide production from water and molecular oxygen by metal-free photocatalysts, *Angew. Chem. Int. Ed.* 53 (2014) 10800–10805.
- [31] Z.Y. Zhang, J.D. Huang, M.Y. Zhang, Q. Yuan, B. Dong, Ultrathin hexagonal SnS_2 nanosheets coupled with $g\text{-C}_3\text{N}_4$ nanosheets as 2D/2D heterojunction photocatalysts toward high photocatalytic activity, *Appl. Catal. B* 163 (2015) 298–305.
- [32] P.Q. Yin, T. Yao, Y. Wu, L.R. Zheng, Y. Lin, W. Liu, H.X. Ju, J.F. Zhu, X. Hong, Z.X. Deng, G. Zhou, S.Q. Wei, Y.D. Li, Single cobalt atoms with precise N-coordination as superior oxygen reduction reaction catalysts, *Angew. Chem. Int. Ed.* 55 (2016) 10800–10805.
- [33] Y.J. Chen, S.F. Ji, Y.G. Wang, J.C. Dong, W.X. Chen, Z. Li, R.G. Shen, L.R. Zheng, Z.B. Zhuang, D.S. Wang, Y.D. Li, Isolated single iron atoms anchored on N-doped porous carbon as an efficient electrocatalyst for the oxygen reduction reaction, *Angew. Chem. Int. Ed.* 56 (2017) 6937–6941.
- [34] Y.B. Wang, D. Cao, X. Zhao, Heterogeneous degradation of refractory pollutants by peroxymonosulfate activated by CoO_x -doped ordered mesoporous carbon, *Chem. Eng. J.* 328 (2017) 1112–1121.
- [35] G.S. Liu, S.J. You, Y. Tan, N.Q. Ren, In situ photochemical activation of sulfate for enhanced degradation of organic pollutants in water, *Environ. Sci. Technol.* 51 (2017) 2339–2346.
- [36] K.-Y.A. Lin, Z.Y. Zhang, Degradation of bisphenol A using peroxymonosulfate activated by one-step prepared sulfur-doped carbon nitride as a metal-free heterogeneous catalyst, *Chem. Eng. J.* 313 (2017) 1320–1327.
- [37] H.F. Li, H.T. Yu, X. Quan, S. Chen, Y.B. Zhang, Uncovering the key role of the Fermi level of the electron mediator in a Z-scheme photocatalyst by detecting the charge transfer process of WO_3 -metal- $g\text{-C}_3\text{N}_4$ (Metal = Cu, Ag, Au), *ACS Appl. Mater. Interfaces* 8 (2016) 2111–2119.
- [38] S.Y. Wang, X. Ding, X.H. Zhang, H. Pang, X. Hai, G.M. Zhan, W. Zhou, H. Song, L.Z. Zhang, H. Chen, J.H. Ye, In situ carbon homogeneous doping on ultrathin bismuth molybdate: a dual-purpose strategy for efficient molecular oxygen activation, *Adv. Funct. Mater.* (2018) 1703923.
- [39] Nabil A. Abdel Ghany, Safaa A. Elsherif, Hala T. Handal, Revolution of Graphene for different applications: state-of-the-art, *Surf. Interfaces* 9 (2017) 93–106.
- [40] C.C. Huang, C. Li, G.Q. Shi, Graphene based catalysts, *Energy Environ. Sci.* 5 (2012) 8848–8868.
- [41] M.Y. Ye, Z.H. Zhao, Z.F. Hu, L.Q. Liu, H.M. Ji, Z.R. Shen, T.Y. Ma, 0D/2D heterojunctions of vanadate quantum dots/graphitic carbon nitride nanosheets for enhanced visible-light-driven photocatalysis, *Angew. Chem. Int. Ed.* 29 (2017) 8407–8411.
- [42] M.Q. Yang, Y.J. Xu, W.H. Lu, K.Y. Zeng, H. Zhu, Q.H. Xu, G.W. Ho, Self-surface charge exfoliation and electrostatically coordinated 2D hetero-layered hybrids, *Nat. Commun.* 8 (2017) 14224.
- [43] W. Liu, L.L. Cao, W.R. Cheng, Y.J. Cao, X.K. Liu, W. Zhang, X.L. Mou, L.L. Jin, X.S. Zheng, W. Che, Q.H. Liu, T. Yao, S.Q. Wei, Single-site active cobalt-based photocatalyst with a long carrier lifetime for spontaneous overall water splitting, *Angew. Chem. Int. Ed.* 56 (2017) 9312–9317.
- [44] R. Shi, H.F. Ye, F. Liang, Z. Wang, K. Li, Y.X. Weng, Z.S. Lin, W.F. Fu, C.M. Che, Y. Chen, Interstitial P-doped CdS with long-lived photogenerated electrons for photocatalytic water splitting without sacrificial agents, *Adv. Mater.* (2018) 1705941.